

# Resonant amplification of multi-messenger emission in rotating stellar core collapse

M. Cusinato,<sup>1,\*</sup> M. Obergaulinger,<sup>1</sup> M.Á. Aloy,<sup>1,2,†</sup> and J.A. Font<sup>1,2</sup>

<sup>1</sup>*Departament d'Astronomia i Astrofísica, Universitat de València, Dr. Moliner, 50, 46100 Burjassot, Spain*

<sup>2</sup>*Observatori Astronòmic, Universitat de València, 46980 Paterna, Spain*

(Dated: April 8, 2025; Received; Accepted)

In a series of axisymmetric core-collapse supernova simulations extending up to  $\sim 2$  s, we identify a regime of pre-collapse central rotation rates ( $\sim 1$  Hz) that greatly enhances the emission of gravitational waves (GWs) during extended periods of time after bounce. The enhancement is a consequence of the resonance between the frequency of the fundamental quadrupolar  $^2f$ -mode of oscillation of the proto-neutron star and the frequency of the epicyclic oscillations at the boundary of the inner core. We observe periods of about several hundred milliseconds each where the resonance is active. The GW emission enhancement produces a correlated resonant modulation of the associated neutrino signal at the same frequencies. With GW frequencies of  $\mathcal{O}(1$  kHz) and strain amplitudes within the sensitivity curves of current and next-generation interferometers at distances of  $\mathcal{O}(1$  Mpc), this resonant-amplification mechanism may represent a potential game-changer for unveiling the supernova explosion mechanism through multi-messenger astronomy.

## INTRODUCTION

Core collapse supernovae (CCSNe) mark the final stage in the evolution of massive stars ( $M_{\text{ZAMS}} \gtrsim 8 M_{\odot}$ ) and are among the prime sources of multimessenger emission as they release gravitational waves (GWs), neutrinos, and electromagnetic signals. The detection of 25 neutrinos from Supernova 1987A [1, 2], along with its electromagnetic counterpart [3, 4], demonstrated that multimessenger observations of CCSNe occurring in the Milky Way are feasible.

Modern neutrino observatories, such as Super-Kamiokande [5], IceCube [6], and KM3NeT [7], are expected to detect tens of thousands of neutrinos from a Galactic CCSN [8] or even the collective contribution of cosmological supernovae to the diffuse supernova neutrino background [9]. On the GW side, advanced detectors like Advanced LIGO [10], Advanced Virgo [11], and KAGRA [12] are sensitive to CCSNe within several kiloparsecs. Despite dedicated efforts by the LIGO–Virgo–KAGRA collaboration to detect CCSNe at distances of up to 30 Mpc, no signals have been recorded [13, 14]. Nonetheless, prospects for detecting extragalactic events remain promising. Future observatories such as Einstein Telescope (ET) [15] and Cosmic Explorer (CE) [16] are expected to substantially extend the detection range, while emerging insights into processes that enhance the amplitude of the GW emission from CCSNe may further improve detection chances.

GWs and neutrinos offer complementary insights into CCSN dynamics. For instance, neutrinos were crucial in estimating the gravitational binding energy released in Supernova 1987A [17]. In contrast, GWs reveal signatures of multidimensional fluid instabilities—including proto-neutron star (PNS) convection [18, 19], stationary accretion shock instability (SASI) [20–22], and prompt convection—emerging during the early stages of the explosion. Moreover, they can constrain the nuclear equation

of state (EOS) [23, 24] and yield estimates of key PNS parameters [25–27].

The rotation of the progenitor star is pivotal in shaping the waveform of the resulting GW signal and, consequently, the detectability of the event [28, 29]. Specifically, when the core of the progenitor star achieves a certain rotational speed, resonances can develop between the PNS oscillation modes and the core’s rotational frequency. Such resonances have been identified in simplified 2-dimensional (2D) models of rotating relativistic stars [30], in the collapse of neutron stars to strange quark stars triggered by phase transitions [31], and during the early phases ( $\lesssim 100$  ms post-bounce) of CCSNe simulations [32]. However, the full evolution of these resonances through the entire operation of the CCSNe engine remains to be comprehensively explored. Previous studies indicate that resonances can notably amplify the GW amplitude, introduce new oscillatory modes, and imprint corresponding signatures in the neutrino signal [32].

In this *Letter* we delve into the rich tapestry of multimessenger signals emerging from CCSN simulations with different initial rotation rates over a span of  $\sim 2$  s. Our findings reveal that when the stellar core rotates at an intermediate rate ( $\approx 1$  Hz), it triggers resonant modes in the PNS that imprint synchronized modulations on the neutrino signal. Remarkably, these resonant GWs generate colossal strains, even surpassing those at bounce, and manifest within mere hundreds of milliseconds after collapse. This striking discovery not only deepens our understanding of the dynamic interplay in stellar explosions but also paves the way for novel insights into their multimessenger signatures.

## METHODS

We performed 2D CCSN simulations using the *Aenus-ALCAR* code [33–35] that couples special relativistic

tic magnetohydrodynamics with a spectral two-moment neutrino transport scheme and incorporates an approximately relativistic gravitational potential [36]. For densities exceeding  $8 \times 10^7 \text{ g/cm}^3$ , we employed the SFHo EOS [37], accounting for photons, electrons, positrons, nucleons, and a full ensemble of light and heavy nuclei in nuclear statistical equilibrium. The GW signal was extracted using the quadrupole formula [38]. The simulations were performed in spherical coordinates on grids with 480 logarithmically spaced radial zones and 128 linearly spaced angular zones, while neutrino energies spanning from 0 MeV to 440 MeV were resolved with 12 logarithmically spaced bins. Each run was evolved for 2 s, commencing from the pre-collapse phase.

After an extensive survey of rotating stellar models evolved to several hundreds of milliseconds post-collapse, we identified a progenitor with a particularly pronounced resonant coupling between GWs and rotation. Specifically, it is a Wolf-Rayet star of subsolar metallicity ( $Z = 0.02 Z_\odot$ ) and zero-age main sequence mass of  $M_{\text{ZAMS}} = 17 M_\odot$ , evolved with both rotation and magnetic fields up to the pre-collapse stage [39]. Its initially high rotational velocity, coupled with enhanced rotational mixing, drives chemically homogeneous evolution. Building on this model, we explored three rotational configurations: the original (SR), with central rotational rate of  $\Omega_c = 0.29 \text{ rad/s}$ , an intermediate case (IR) with a rate amplified by a factor of 3.5, and a fast-rotating scenario (FR) with a 12-fold increase. Although these increased rotation rates are substantial, they remain well within the computed range for massive stars [40, 41].

## RESULTS

The plus polarisation of the GW signal,  $h_+$ , for a source at distance  $\mathcal{D}$  (see top panel of Figure 1) reveals the brief yet intense bounce signal characteristic of rapidly rotating cores [43, 44]. In the most rapidly rotating model FR, the signal amplitude reaches  $\mathcal{D}h_+ \gtrsim 100 \text{ cm}$ . Following the bounce, the waveform transitions into a regime of weaker oscillations that remain centered around zero in model SR or gradually drift towards positive values in models IR and FR, which ultimately explode via polar jets.

Unlike models SR and FR, where the oscillatory amplitudes remain relatively constant throughout the simulation, model IR undergoes two distinct phases of pronounced amplitude enhancement, the first occurring between  $t \approx 0.4 \text{ s}$  and  $0.8 \text{ s}$ , and the second one between  $t \approx 1.1 \text{ s}$  and  $1.4 \text{ s}$ . During these bursts, the strain range widens to approximately  $\sim 130 \text{ cm}$  and  $\sim 300 \text{ cm}$ , respectively, reaching levels comparable to the bounce signal observed in model FR.

The bottom panel of Figure 1 shows the GW spectrogram of model IR, computed using a short-time Fourier

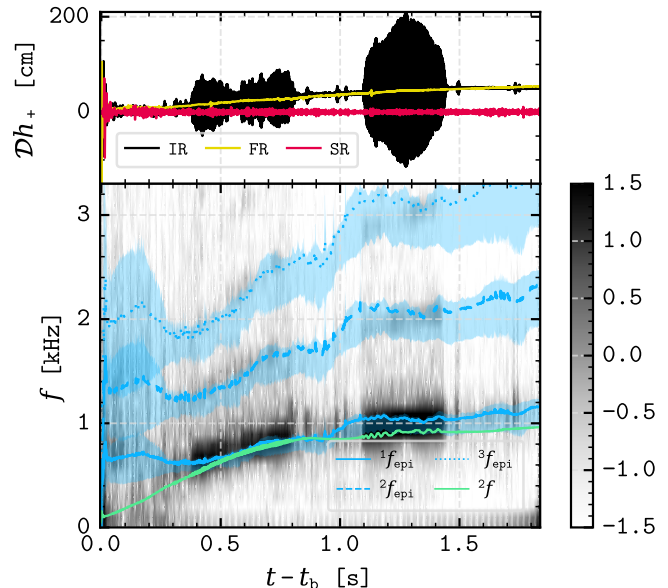


FIG. 1. Top panel: GW strains emitted by a source at distance  $\mathcal{D}$  for models SR (red), IR (black), and FR (yellow). Bottom panel: Spectrogram of the GW signal for model IR. Blue lines represent the fundamental frequency (solid), the first (dashed) and the second (dotted) overtones of the epicyclic frequency, with shaded regions showing the associated uncertainties. The green line indicates the fundamental quadrupolar mode, computed using the quasi-universal relation from [42].

transform with a 10 ms time window. The two GW bursts display distinct spectral evolutions: the first rises from  $\sim 550 \text{ Hz}$  to  $\sim 1 \text{ kHz}$ , while the second steadily hovers near 1 kHz. These frequencies align with the predicted fundamental quadrupolar  $^2f$ -mode (green line; see, e.g., [27, 42]). Moreover, additional harmonics appear at twice and thrice these frequencies, albeit with progressively lower amplitudes.

Using the quadrupole formula, we pinpoint the origin of the GW strain to the innermost part of the star (hereafter PNS core), which we defined as the region within the iso-entropy surface at  $4k_B/\text{bry}$  [45], corresponding to a radius of  $r_{\text{core}} \sim 20 \text{ km}$ ). The pronounced high-amplitude emission arises from a resonant interplay between PNS modes and rotation. The centrifugal force causes fluid elements within the PNS core to oscillate in the direction of the cylindrical radial distance. To quantify these oscillations, we use the epicyclic frequency, defined as

$${}^n f_{\text{epi}} = \frac{n}{2\pi} \sqrt{\frac{2\Omega}{R} \frac{d(\Omega R^2)}{dR}}, \quad (1)$$

where  $n$  is the overtone number,  $R$  the cylindrical radius, and  $\Omega$  the angular velocity.

Within the PNS core, we focus on a conical region spanning the colatitude range  $[15^\circ, 85^\circ]$ . At each radius,

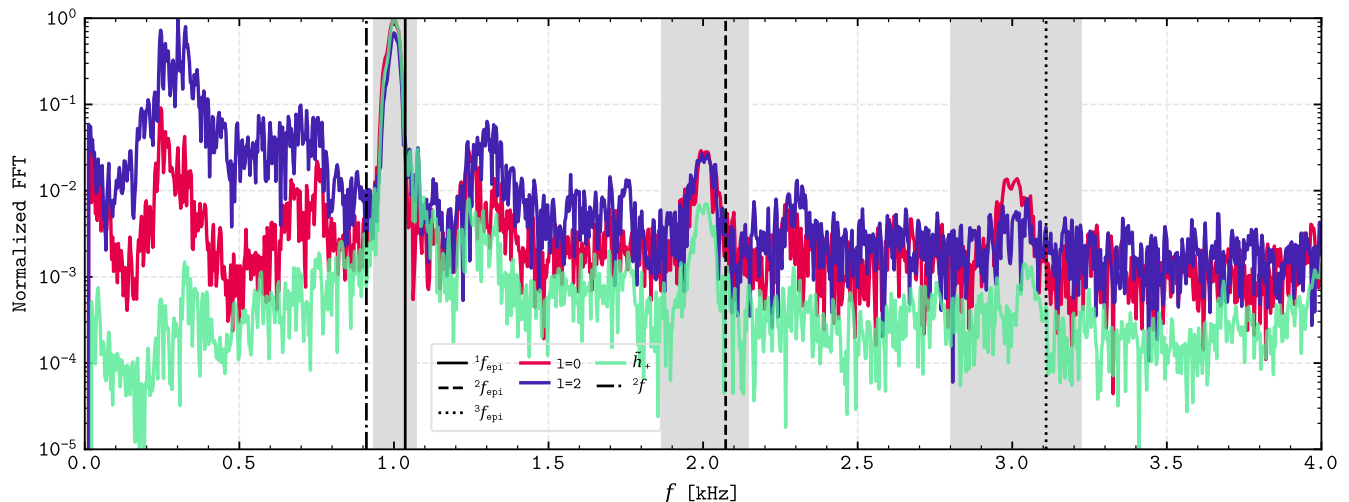


FIG. 2. Normalized Fourier transform of the equatorial density ( $l = 0$ ),  $v_\theta$  at  $\pi/4$  ( $l = 2$ ), both outside of taken the PNS core outer boundary at 25 km, and of the GW signal ( $\tilde{h}_+$ ) for the time interval 1.1 – 1.4 s. The solid, dashed, and dotted black vertical lines represent the fundamental frequency and the first and second overtones of the average epicyclic frequency, respectively. Shaded regions indicate the uncertainty associated with the frequencies. The dash-dotted line represents the average  $^2f$ -mode frequency derived with the relations in [42].

we determine the maximum epicyclic frequency and subsequently compute the average and standard deviation of these maxima. This specific colatitude range was chosen to exclude the polar region (prone to numerical artifacts in axial symmetry) and the equator, where converging convective flows compromise the accuracy of the  $^n f_{\text{epi}}$  evaluation. Recognizing that simply taking the maximum may lead to an overestimate, we conservatively define the lower uncertainty as the largest value between the standard deviation and 10% of the maximum of the epicyclic frequency. The bottom panel of Figure 1 shows the evolution of these averages (blue lines) and uncertainties (shades) for  $^1 f_{\text{epi}}$  (solid),  $^2 f_{\text{epi}}$  (dashed), and  $^3 f_{\text{epi}}$  (dotted).

Resonance occurs when the fundamental epicyclic frequency intersects or comes sufficiently close to the  $^2 f$ -mode frequency. To give a first analytic estimate of the latter we employ the quasi-universal relations of [42]. Although these relations were obtained from non-rotating 1D CCSN simulations and thus may exhibit minor deviations from our models, they still provide a useful point of reference for comparison with the epicyclic frequency.

To further validate the resonance mechanism, we resort to the computed data to give a second estimate of the frequency of the quasi-radial ( $l = 0$ ) and quadrupolar ( $l = 2$ ) modes. As in [30], we use as proxies for the amplitudes of the  $l = 0$  and  $l = 2$  modes the real parts of the Fourier spectra of the mass density at  $r = 25$  km,  $\theta = \pi/2$  and of  $v_\theta$  at  $r = 25$  km,  $\theta = \pi/4$ , respectively. In Figure 2 we present the Fourier transform amplitude of the GW, density and  $v_\theta$ , each normalized by their maximum during the second resonant phase (1.15 – 1.45 s). The

GW spectrum (green line) exhibits a series of distinct peaks starting at  $\sim 1$  kHz, spaced at intervals of  $\sim 1$  kHz. These peaks persist up to  $\sim 7$  kHz, though their amplitude steadily diminishes with increasing frequency, a behaviour indicative of overtones of the epicyclic frequency.

The spectral peaks of the  $l = 0$  mode (red line) and  $l = 2$  (blue line) closely align with those of the epicyclic frequency and its overtones. The slight shift between the local GW spectral peak spectrum and the epicyclic frequency is likely due to its overestimation. Furthermore, the first peak in the GW spectrum, corresponding to the fundamental epicyclic frequency, agrees with the  $^2 f$ -mode estimated via the quasi-universal relations of [42]. Together, these findings suggest that the fundamental epicyclic mode is the primary driver of the observed GW emission during the resonant phase.

To assess the detectability of the GW signal, we compute its characteristic strain [46],  $h_{\text{char}}$ ,

$$h_{\text{char}}(f) = \frac{1}{\pi \mathcal{D}} \sqrt{\frac{2G}{c^3} \frac{dE}{df}}, \quad (2)$$

where  $c$  is the speed of light,  $G$  is the gravitational constant, and  $\frac{dE}{df}$  denotes the time-integrated energy spectrum. In Figure 3 we show  $h_{\text{char}}/f^{1/2}$  for models SR, IR, and FR at  $\mathcal{D} = 1$  Mpc, juxtaposed with the amplitude spectral density (ASD) of current and next-generation interferometers, namely Advanced LIGO [47, 48], Advanced Virgo [47, 48], KAGRA [47, 48], ET [49, 50], and CE [51, 52].

Model SR notably exhibits a broad low-frequency hump

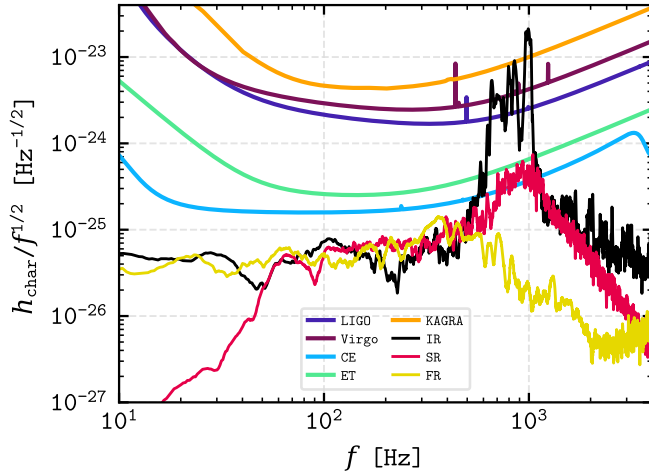


FIG. 3. Characteristic GW spectra for models SR (red), IR (black), and FR (yellow), assuming a source distance of 1 Mpc, compared with the design sensitivity curves of current and next-generation interferometers.

spanning 40 – 90 Hz alongside a broad high-frequency peak at 400 – 1000 Hz. While the low-frequency features fall below the sensitivity range of present and future detectors, the high-frequency peak marginally surpasses the theoretical sensitivity of CE. Moreover, in the absence of polar jets, no significant power is observed below  $f \sim 30$  Hz.

Model FR exhibits a broad plateau below 250 Hz. Its high-frequency peak is shifted down to  $\sim 400$  Hz and is markedly weaker compared to models SR and IR. Contrary to the previous model, a spectral power excess at low frequencies ( $\lesssim 30$  Hz), is present, indicating jet formation.

Model IR differs significantly from the others. It displays two low-frequency spectral humps: one at intermediate frequencies (60 – 200 Hz, and another below 30 Hz). The most striking feature of IR is the unmistakable resonance imprint on its characteristic strain. This model yields the strongest signal, with a peak strain more than twice that observed in SR—translating into a peak ASD more than 10 (100) times larger than in model SR (FR)—(see Figure 3). Four prominent peaks, spanning from  $\sim 600$  Hz to  $\sim 1$  kHz, mark the resonant frequencies during the first and second resonant phases (see Figure 1). Remarkably, even at a distance of 1 Mpc, these features lie within the detection range of current interferometers like Advanced LIGO and Virgo, with next-generation detectors promising even greater sensitivity. Overtones at  $f \gtrsim 2$  kHz and  $f \gtrsim 3$  kHz are also present.

In model IR, the neutrino emission shows resonant features at frequencies matching those of the GWs signal, albeit at slightly lower amplitudes. These resonant imprints emerge in the mean energies and luminosities of all three neutrino flavours ( $\nu_e$ ,  $\bar{\nu}_e$ , and the combined  $\tau$ –

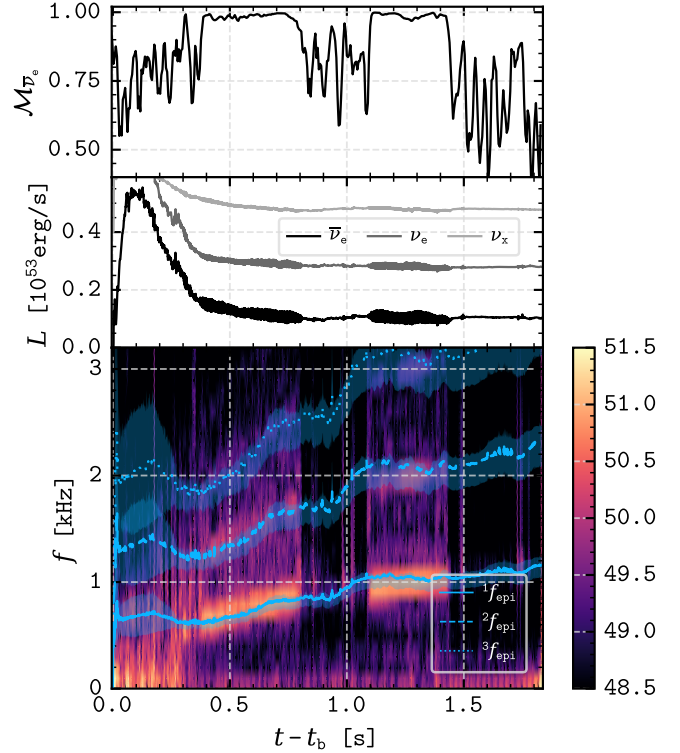


FIG. 4. Top panel: evolution of the matching score between the spectrograms of the  $\bar{\nu}_e$  and GW signals. Middle panel: neutrino luminosities of electron antineutrinos (black line), electron neutrinos (dark gray, shifted by  $0.2 \times 10^{53}$  erg/s), heavy lepton neutrinos (light gray, shifted by  $0.4 \times 10^{53}$  erg/s). Bottom panel: spectrogram of the antineutrino luminosities, with the shaded regions and blue lines denoting the same quantities as in Figure 1. Both panels refer to model IR.

and  $\mu$ –neutrinos,  $\nu_x$ ). The two bottom panels of Figure 4 depict, respectively, the evolution of the global neutrino luminosity (middle panel) and the spectrogram of the electron antineutrino luminosity (bottom panel), both computed with a 10 ms time window, analogous to the analysis conducted for the GW signal.

During the resonance intervals observed in the GW signal (0.4 – 0.8 s and 1.1 – 1.4 s), the global neutrino luminosity oscillates around its mean value. Although such oscillations are evident in all neutrino flavours, the resonance imprint is most pronounced in the  $\bar{\nu}_e$  component, followed by  $\nu_e$ , and is least apparent in  $\nu_x$  signal. The spectrogram of the  $\bar{\nu}_e$  luminosity (bottom panel of Figure 4) mirrors that of the GWs, displaying two distinct phases of robust, resonantly excited oscillations at the epicyclic frequency or its overtones (blue lines).

To quantify the correlation between the GW and neutrino signals, we use the matching score [53],

$$\mathcal{M}_{\nu_i}(t) = \frac{\langle S_{\text{GW}}(f, t) | S_{\nu_i}(f, t) \rangle}{\sqrt{\langle S_{\text{GW}}(f, t) | S_{\text{GW}}(f, t) \rangle \langle S_{\nu_i}(f, t) | S_{\nu_i}(f, t) \rangle}}, \quad (3)$$

where  $S_j(f, t)$  ( $j = \text{GW}, \nu_i$ ) denotes the magnitude of the spectrogram computed with a 10 ms time window, and  $\langle \cdot | \cdot \rangle$  represents the inner product in frequency space.

The top panel of Figure 4 depicts the evolution of the matching score between the GWs (bottom panel of Figure 1) and  $\bar{\nu}_e$  spectrograms (bottom panel of Figure 4; results for the other flavours are similar) for frequencies above 200 Hz, a threshold set to minimize stochastic contributions from convection and SASI. Throughout the simulation, the matching score consistently exceeds 0.6. Notably, during the two resonant phases (0.4 – 0.8 s and 1.1 – 1.4 s), it approaches unity, unequivocally demonstrating that the amplitude modulations in both signals are correlated and originate from the same rotationally driven oscillations of the PNS core.

## DISCUSSION AND CONCLUSIONS

We have reported results from 2D CCSN simulations for a model with a pre-bounce central rotation rate of  $\Omega_c \sim 1$  rad/s that reveal extended intervals—lasting several hundred milliseconds—of extraordinarily strong GW emission. Such pronounced signals are absent in otherwise identical progenitors with either slower or faster initial rotation. We attribute this enhanced emission to a resonance between the frequency of the fundamental quadrupolar  $^2f$ -mode and the frequency of epicyclic oscillations at the outer boundary of the PNS inner core. Notably, while the GW amplitudes are comparable to the bounce signals observed in rapidly rotating cores, they persist for much longer. Crucially, the resonance signatures dominate the most prominent features of the characteristic strain, and their typical frequencies of around 1 kHz renders them compelling targets for ground-based GW detectors. Although higher harmonics are also excited, their detection is impeded by both their high frequencies and lower amplitudes. We also detect imprints of these resonant oscillations in the neutrino emission from the core, with luminosities and mean energies modulated at the same frequencies, most prominently in the  $\bar{\nu}_e$  and  $\nu_e$  channels.

While our findings are highly promising for multi-messenger observations of CCSNe, further investigation is clearly warranted. In realistic CCSN cores, deviations from axisymmetry arise rapidly; at the rotation rates explored here, non-axisymmetric instabilities may develop and alter the rotational profile, potentially modifying the conditions for resonance. These effects must be rigorously examined using full 3-dimensional (3D) simulations. Furthermore, future studies should probe whether this resonance is sensitive to other progenitor properties, such as initial mass or metallicity, and if it can offer new constraints on the nuclear EOS.

Bearing in mind these caveats, the pronounced, long-lasting modulation of the GW signal induced by reso-

nance reported in this work could represent a breakthrough for multi-messenger detections of CCSNe. Given the substantial GW amplitude enhancement, this resonant signature should remain detectable at distances of  $\mathcal{O}(1 \text{ Mpc})$  or, with CE, even  $\mathcal{O}(30 \text{ Mpc})$ , rendering it a compelling target for both current and next-generation interferometers. Using the CCSN rate estimate [54], the most optimistic source distance of 30 Mpc, and a conservative appraisal that approximately 2% of all the massive stars rotate at rates of around 1 Hz [55], our findings indicate that future detectors could routinely observe  $\sim 1$  CCSN per year.

*Acknowledgements.* We acknowledge the support through the grants PID2021-127495NB-I00 and PID2021-125485NB-C21 funded by MCIN/AEI/10.13039/501100011033 and by the European Union, and the Astrophysics and High Energy Physics programme of the Generalitat Valenciana ASFAE/2022/026 funded by MCIN and the European Union NextGenerationEU (PRTR-C17.I1) as well as support from the Prometeo excellence programme grants CIPROM/2022/13 and CIPROM/2022/49 funded by the Generalitat Valenciana. MO was supported by the Ramón y Cajal programme of the Agencia Estatal de Investigación (RYC2018-024938-I).

---

\* marco.cusinato@uv.es

† miguel.a.aloy@uv.es

- [1] R. M. Bionta, G. Blewitt, C. B. Bratton, D. Casper, A. Ciocio, R. Claus, B. Cortez, M. Crouch, S. T. Dye, S. Errede, G. W. Foster, W. Gajewski, K. S. Ganezer, M. Goldhaber, T. J. Haines, T. W. Jones, D. Kielczewska, W. R. Kropp, J. G. Learned, J. M. Losecco, J. Matthews, R. Miller, M. S. Mudan, H. S. Park, L. R. Price, F. Reines, J. Schultz, S. Seidel, E. Shumard, D. Sinclair, H. W. Sobel, J. L. Stone, L. R. Sulak, R. Svoboda, G. Thornton, J. C. van der Velde, and C. Wuest, *Phys. Rev. Lett.* **58**, 1494 (1987).
- [2] K. Hirata, T. Kajita, M. Koshiba, M. Nakahata, Y. Oyama, N. Sato, A. Suzuki, M. Takita, Y. Totsuka, T. Kifune, T. Suda, K. Takahashi, T. Tanimori, K. Miyano, M. Yamada, E. W. Beier, L. R. Feldscher, S. B. Kim, A. K. Mann, F. M. Newcomer, R. van, W. Zhang, and B. G. Cortez, *Phys. Rev. Lett.* **58**, 1490 (1987).
- [3] T. Dotani, K. Hayashida, H. Inoue, M. Itoh, K. Koyama, F. Makino, K. Mitsuda, T. Murakami, M. Oda, Y. Ogawara, S. Takano, Y. Tanaka, A. Yoshida, K. Makishima, T. Ohashi, N. Kawai, M. Matsuoka, R. Hoshi, S. Hayakawa, T. Kii, H. Kuniieda, F. Nagase, Y. Tawara, I. Hatsukade, S. Kitamoto, S. Miyamoto, H. Tsunemi, K. Yamashita, M. Nakagawa, M. Yamauchi, M. J. L. Turner, K. A. Pounds, H. D. Thomas, G. C. Stewart, A. M. Cruise, B. E. Patchett, and D. H. Reading, *Nature* **330**, 230 (1987).
- [4] S. M. Matz, G. H. Share, M. D. Leising, E. L. Chupp, W. T. Vestrand, W. R. Purcell, M. S. Strickman, and

- C. Reppin, *Nature* **331**, 416 (1988).
- [5] K. Scholberg, *Annual Review of Nuclear and Particle Science* **62**, 81 (2012), arXiv:1205.6003 [astro-ph.IM].
- [6] The IceCube Collaboration, *Journal of Instrumentation* **12**, P03012 (2017), arXiv:1612.05093 [astro-ph.IM].
- [7] KM3NeT Collaboration, *Journal of Physics G Nuclear Physics* **43**, 084001 (2016), arXiv:1601.07459 [astro-ph.IM].
- [8] Y. Suwa, A. Harada, M. Harada, Y. Koshio, M. Mori, F. Nakanishi, K. Nakazato, K. Sumiyoshi, and R. A. Wendell, *ApJ* **934**, 15 (2022), arXiv:2204.08363 [astro-ph.HE].
- [9] P. Martínez-Miravé, I. Tamborra, M. Á. Aloy, and M. Obergaulinger, *Phys. Rev. D* **110**, 103029 (2024), arXiv:2409.09126 [astro-ph.HE].
- [10] LIGO Scientific Collaboration, *Classical and Quantum Gravity* **32**, 074001 (2015), arXiv:1411.4547 [gr-qc].
- [11] V. S. Collaboration, *Classical and Quantum Gravity* **32**, 024001 (2014).
- [12] KAGRA Scientific Collaboration, *Nature Astronomy* 2019 3:1 **3**, 35 (2019).
- [13] M. J. Szczepańczyk, Y. Zheng, J. M. Antelis, M. Benjamin, M.-A. Bizouard, A. Casallas-Lagos, P. Cerdá-Durán, D. Davis, D. Gondek-Rosińska, S. Klimenko, C. Moreno, M. Obergaulinger, J. Powell, D. Ramirez, B. Ratto, C. Richardson, A. Rijal, A. L. Stuver, P. Szcwyczyk, G. Vedovato, M. Zanolin, I. Bartos, S. Bhaumik, T. Bulik, M. Drago, J. A. Font, F. De Colle, J. García-Bellido, V. Gayathri, B. Hughey, G. Mitselmakher, T. Mishra, S. Mukherjee, Q. L. Nguyen, M. L. Chan, I. Di Palma, B. J. Piotrkowski, and N. Singh, *Phys. Rev. D* **110**, 042007 (2024), arXiv:2305.16146 [astro-ph.HE].
- [14] The LIGO Scientific Collaboration, the Virgo Collaboration, and the KAGRA Collaboration, arXiv e-prints, arXiv:2410.16565 (2024), arXiv:2410.16565 [astro-ph.HE].
- [15] M. Maggiore, C. Van Den Broeck, N. Bartolo, E. Belgacem, D. Bertacca, M. A. Bizouard, M. Branchesi, S. Clesse, S. Foffa, J. García-Bellido, S. Grimm, J. Harms, T. Hinderer, S. Matarrese, C. Palomba, M. Peloso, A. Ricciardone, and M. Sakellariadou, *J. Cosmology Astropart. Phys.* **2020**, 050 (2020), arXiv:1912.02622 [astro-ph.CO].
- [16] D. Reitze, R. X. Adhikari, S. Ballmer, B. Barish, L. Barsotti, G. Billingsley, D. A. Brown, Y. Chen, D. Coyne, R. Eisenstein, M. Evans, P. Fritschel, E. D. Hall, A. Lazzarini, G. Lovelace, J. Read, B. S. Sathyaprakash, D. Shoemaker, J. Smith, C. Torrie, S. Vitale, R. Weiss, C. Wipf, and M. Zucker, in *Bulletin of the American Astronomical Society*, Vol. 51 (2019) p. 35, arXiv:1907.04833 [astro-ph.IM].
- [17] A. Burrows, *ApJ* **334**, 891 (1988).
- [18] B. Müller, H.-T. Janka, and A. Marek, *ApJ* **766**, 43 (2013), arXiv:1210.6984 [astro-ph.SR].
- [19] K.-C. Pan, M. Liebendörfer, S. M. Couch, and F.-K. Thielemann, *ApJ* **857**, 13 (2018), arXiv:1710.01690 [astro-ph.HE].
- [20] P. Cerdá-Durán, N. DeBrye, M. A. Aloy, J. A. Font, and M. Obergaulinger, *ApJ* **779**, L18 (2013), arXiv:1310.8290 [astro-ph.SR].
- [21] A. Torres-Forné, P. Cerdá-Durán, A. Passamonti, and J. A. Font, *MNRAS* **474**, 5272 (2018).
- [22] H. Andresen, B. Müller, E. Müller, and H. T. Janka, *MNRAS* **468**, 2032 (2017), arXiv:1607.05199 [astro-ph.HE].
- [23] T. Malik, N. Alam, M. Fortin, C. Providência, B. K. Agrawal, T. K. Jha, B. Kumar, and S. K. Patra, *Phys. Rev. C* **98**, 035804 (2018).
- [24] G. Raaijmakers, S. K. Greif, T. E. Riley, T. Hinderer, K. Hebeler, A. Schwenk, A. L. Watts, S. Nisanke, S. Guillot, J. M. Lattimer, and R. M. Ludlam, *ApJ* **893**, L21 (2020), arXiv:1912.11031 [astro-ph.HE].
- [25] A. Torres-Forné, P. Cerdá-Durán, M. Obergaulinger, B. Müller, and J. A. Font, *Phys. Rev. Lett.* **123**, 051102 (2019).
- [26] T. Bruel, M.-A. Bizouard, M. Obergaulinger, P. Maturana-Russel, A. Torres-Forné, P. Cerdá-Durán, N. Christensen, J. A. Font, and R. Meyer, *Phys. Rev. D* **107**, 083029 (2023), arXiv:2301.10019 [astro-ph.HE].
- [27] M. C. Rodriguez, I. F. Ranea-Sandoval, C. Chirenti, and D. Radice, *Mon. Not. Roy. Astron. Soc.* **523**, 2236 (2023).
- [28] S. Shibagaki, T. Kuroda, K. Kotake, T. Takiwaki, and T. Fischer, *MNRAS* **531**, 3732 (2024), arXiv:2309.05161 [astro-ph.HE].
- [29] J. Powell and B. Müller, *MNRAS* **532**, 4326 (2024), arXiv:2406.09691 [astro-ph.HE].
- [30] H. Dimmelmeier, N. Stergioulas, and J. A. Font, *MNRAS* **368**, 1609 (2006).
- [31] E. B. Abdikamalov, H. Dimmelmeier, L. Rezzolla, and J. C. Miller, *MNRAS* **392**, 52 (2009), arXiv:0806.1700 [astro-ph].
- [32] J. R. Westernacher-Schneider, E. O'Connor, E. O'Sullivan, I. Tamborra, M.-R. Wu, S. M. Couch, and F. Malmenbeck, *Phys. Rev. D* **100**, 123009 (2019), arXiv:1907.01138 [astro-ph.HE].
- [33] M. Obergaulinger, O. Just, and M. A. Aloy, *Journal of Physics G Nuclear Physics* **45**, 084001 (2018).
- [34] O. Just, M. Obergaulinger, and H. T. Janka, *MNRAS* **453**, 3386 (2015), arXiv:1501.02999 [astro-ph.HE].
- [35] M. Obergaulinger and M. Á. Aloy, *MNRAS* **512**, 2489 (2022).
- [36] A. Marek, H. Dimmelmeier, H. T. Janka, E. Müller, and R. Buras, *A&A* **445**, 273 (2006), arXiv:astro-ph/0502161 [astro-ph].
- [37] A. W. Steiner, J. M. Lattimer, and E. F. Brown, *ApJ* **765**, L5 (2013), arXiv:1205.6871 [nucl-th].
- [38] M. Obergaulinger, M. A. Aloy, and E. Müller, *A&A* **450**, 1107 (2006), arXiv:astro-ph/0510184 [astro-ph].
- [39] D. R. Aguilera-Dena, N. Langer, T. J. Moriya, and A. Schootemeijer, *ApJ* **858**, 115 (2018), arXiv:1804.07317 [astro-ph.SR].
- [40] S. E. Woosley and A. Heger, *ApJ* **637**, 914 (2006), arXiv:astro-ph/0508175 [astro-ph].
- [41] A. Griffiths, P. Eggenberger, G. Meynet, F. Moyano, and M.-Á. Aloy, *A&A* **665**, A147 (2022), arXiv:2204.00016 [astro-ph.SR].
- [42] A. Torres-Forné, P. Cerdá-Durán, A. Passamonti, M. Obergaulinger, and J. A. Font, *MNRAS* **482**, 3967 (2019).
- [43] E. Abdikamalov, S. Gossan, A. M. DeMaio, and C. D. Ott, *Phys. Rev. D* **90**, 044001 (2014), arXiv:1311.3678 [astro-ph.SR].
- [44] S. Richers, C. D. Ott, E. Abdikamalov, E. O'Connor, and C. Sullivan, *Phys. Rev. D* **95**, 063019 (2017), arXiv:1701.02752 [astro-ph.HE].
- [45] T. Ertl, H. T. Janka, S. E. Woosley, T. Sukhbold, and

- M. Ugliano, *ApJ* **818**, 124 (2016).
- [46] É. É. Flanagan and S. A. Hughes, *Phys. Rev. D* **57**, 4535 (1998).
- [47] L. S. C. KAGRA Collaboration and VIRGO Collaboration, *Living Reviews in Relativity* **23**, 3 (2020).
- [48] L. S. C. KAGRA Collaboration and VIRGO Collaboration, “Noise curves used for Simulations in the update of the Observing Scenarios Paper,” <https://dcc.ligo.org/LIGO-T2000012/public> (2022), online; accessed January 2025.
- [49] S. Hild and others, *Classical and Quantum Gravity* **28**, 094013 (2011), arXiv:1012.0908 [gr-qc].
- [50] ET design team, “ET-D sensitivity curve,” <https://apps.et-gw.eu/tds/?content=3&r=14065> (2018), online; accessed January 2025.
- [51] V. Srivastava, D. Davis, K. Kuns, P. Landry, S. Ballmer, M. Evans, E. D. Hall, J. Read, and B. S. Sathyaprakash, *ApJ* **931**, 22 (2022), arXiv:2201.10668 [gr-qc].
- [52] Kuns, Kevin and Fulda, Paul and Barsotti, Lisa and Evans, Matthew, “Cosmic Explorer Document T2000017-v8,” <https://dcc.cosmicexplorer.org/CE-T2000017/public> (2023), online; accessed January 2025.
- [53] S. Suvorova, J. Powell, and A. Melatos, *Phys. Rev. D* **99**, 123012 (2019), arXiv:1901.02535 [astro-ph.IM].
- [54] F. Mannucci, D. Maoz, K. Sharon, M. T. Botticella, M. Della Valle, A. Gal-Yam, and N. Panagia, *MNRAS* **383**, 1121 (2008), arXiv:0710.1094 [astro-ph].
- [55] G. Holgado, S. Simón-Díaz, A. Herrero, and R. H. Barbá, *A&A* **665**, A150 (2022), arXiv:2207.12776 [astro-ph.SR].